Available online at www.sciencedirect.com
SCIENCE DIRECT®
Journal of Power Sources 141 (2005) 79–95
JOURNAL OF POWER SOURCES
www.elsevier.com/locate/jpowsour

Dependence of polarization in anode-supported solid oxide fuel cells on various cell parameters

Feng Zhao, Anil V. Virkar*

Department of Materials Science and Engineering, 122 S. Central Campus Drive, University of Utah, Salt Lake City, UT 84112, USA

Received 9 August 2003; received in revised form 31 August 2004; accepted 31 August 2004

Abstract

The performance of solid oxide fuel cells (SOFCs) is affected by various polarization losses, namely, ohmic polarization, activation polarization and concentration polarization. Under given operating conditions, these polarization losses are largely dependent on cell materials, electrode microstructures, and cell geometric parameters. Solid oxide fuel cells (SOFC) with yttria-stabilized zirconia (YSZ) electrolyte, Ni–YSZ anode support, Ni–YSZ anode interlayer, strontium doped lanthanum manganate (LSM)–YSZ cathode interlayer, and LSM current collector, were fabricated. The effect of various parameters on cell performance was evaluated. The parameters investigated were: (1) YSZ electrolyte thickness, (2) cathode interlayer thickness, (3) anode support thickness, and (4) anode support porosity. Cells were tested over a range of temperatures between 600 and 800 °C with hydrogen as fuel, and air as oxidant. Ohmic contribution was determined using the current interruption technique. The effect of these cell parameters on ohmic polarization and on cell performance was experimentally measured. Dependence of cell performance on various parameters was rationalized on the basis of a simple analytical model. Based on the results of the cell parameter study, a cell with optimized parameters was fabricated and tested. The corresponding maximum power density at 800 °C was ~1.8 W cm^{-2}.

Keywords: Anode supported; Solid oxide fuel cells; Cell parameters; Polarization; Current interruption

1. Introduction

In solid oxide fuel cell (SOFC) research, the anode-supported design has been extensively investigated in recent years. This is because anode-supported SOFCs can be fabricated with relative ease, are mechanically rugged, and exhibit some of the highest power densities at temperatures as low as 750 °C. Power densities in excess of 1 W cm^{-2} at the operating temperatures have been reported [1–3].

Although significant strides have been made in recent years in improving cell performance, there is still considerable room for further improvements, even with the standard materials set comprising Y_2O_3-stabilized zirconia (YSZ) as the electrolyte and a constituent in the composite anode and cathode, Ni for the anode, and Sr-doped $LaMnO_3$ (LSM) for the cathode. Even greater improvements are deemed possible with other materials for electrode and electrolyte with intrinsically superior properties. For this reason, much work is currently underway in this area.

There are five loss mechanisms, which result in the loss of useful voltage of a cell at a given operating current density. They are: (1) ohmic polarization, which is the voltage loss due to the ohmic resistances of the electrolyte, electrodes and interfaces between the electrodes and the electrolyte, and between the electrodes and the current collectors (contact resistance). (2) Concentration polarization at the cathode, which is the voltage loss associated with the transport of gaseous oxidant through the porous cathode. (3) Activation polarization at the cathode, which is the voltage loss associated with the oxygen reduction reaction. (4) Concentration polarization at the anode, which is the voltage loss associated with

* Corresponding author. Tel.: +1 801 581 5396; fax: +1 801 581 4816.
E-mail address: anil.virkar@m.cc.utah.edu (A.V. Virkar).

0378-7753/$ – see front matter © 2004 Elsevier B.V. All rights reserved.
doi:10.1016/j.jpowsour.2004.08.057

the transport of gaseous fuel through the anode. (5) Activation polarization at the anode, which is the voltage loss associated with the hydrogen oxidation reaction. The total polarization, η_{total}, can be expressed as

$$\eta_{\text{total}} = \eta_{\text{electrode}} + \eta_{\text{ohmic}} = \eta_{\text{a,act}} + \eta_{\text{a,con}} + \eta_{\text{c,act}} + \eta_{\text{c,con}} + \eta_{\text{ohmic}} \quad (1)$$

where $\eta_{\text{electrode}}$ is the sum of activation and concentration polarizations at the two electrodes, $\eta_{\text{a,act}}$ and $\eta_{\text{a,con}}$ are respectively, activation and concentration polarizations at the anode, $\eta_{\text{c,act}}$ and $\eta_{\text{c,con}}$ are respectively, activation and concentration polarizations at the cathode, and η_{ohmic} is the total ohmic polarization. An efficient operation of SOFC requires that all of these losses be as small as possible. Parameters such as the ionic conductivity of the electrolyte and electronic and ionic conductivities of the two electrodes, the thicknesses of the electrolyte and electrodes, and possible ohmic resistances associated with interfaces, determine the ohmic loss. It is often assumed that most of the ohmic loss is due to the electrolyte. Thus, a high ionic conductivity and a small electrolyte thickness are the desired characteristics of the solid electrolyte to minimize the ohmic contribution. Although various solid electrolytes with high ionic conductivities at moderate temperatures have been explored, yttria-stabilized zirconia (YSZ) is by far the most widely used solid electrolyte due to its excellent stability in both reducing and oxidizing environments, even though its conductivity is lower than other materials such as ceria and Sr- and Mg-doped $LaGaO_3$ (LSGM). Higher conductivity electrodes and lower sheet resistance are also important in lowering the ohmic contribution. Insofar as electrodes are concerned, the ohmic contribution also depends upon the relative amounts of the two phases present, the amount of porosity, and microstructure—in particular the geometry of the particle to particle contact. Parameters such as the electrode porosity, the pore size and the pore morphology (which affects the totuosity factor) influence the transport of gaseous species through the electrodes and thus the accompanying concentration polarization. Finally, the electrode interlayer morphology, including the three phase boundary (TPB) length, determine the activation polarization.

In addition to these electrode microstructure-related parameters, the electrode thickness is also expected to affect concentration polarization; the thicker is the support electrode, the greater is the concentration polarization. From the standpoint of ruggedness and mechanical integrity, the electrode should be of a sufficient thickness. From the standpoint of concentration polarization, however, the thinner is the electrode, the lower is the concentration polarization. It is thus necessary to determine how thick the electrode support should be without significantly increasing concentration polarization losses.

Within a given set of materials, such as YSZ electrolyte, Sr-doped $LaMnO_3$ (LSM) cathode, and Ni + YSZ anode, large variability in performance characteristics can occur depending upon the geometric design of the fuel cell and the microstructural and compositional parameters of the electrodes. For the present study the materials selected were LSM of composition $La_{0.85}Sr_{0.15}MnO_{(3-\delta)}$ for the cathode interlayer and cathode current collector, Ni for the anode interlayer and anode support, and YSZ of composition 8 mol.% Y_2O_3–92 mol.% ZrO_2, for the electrolyte, for the LSM + YSZ cathode interlayer, for the Ni + YSZ anode interlayer, and for the Ni + YSZ anode support. The cathode interlayer, where most of the electrocatalysis related to oxygen reduction occurs was a porous composite of LSM + YSZ. The anode interlayer, where most of the electrocatalysis related to hydrogen oxidation occurs was a porous composite of Ni + YSZ. The relative proportions of LSM and YSZ in cathode interlayer, and Ni and YSZ in anode interlayer and anode support, were fixed in all experiments. The principal objective of the present work was to experimentally study the effect of electrolyte thickness, anode support thickness, anode support porosity, and cathode interlayer thickness on cell performance. Button cells were fabricated with one parameter varied at a time, keeping other parameters fixed. Cells were subsequently tested with humidified hydrogen as fuel and air as oxidant.

2. Experimental procedure

2.1. Cell fabrication

A typical cell used in the present work consisted of the following five distinct layers. (a) Porous Ni + YSZ anode support. (b) Porous Ni + YSZ anode interlayer. (c) Dense YSZ electrolyte. (d) Porous LSM + YSZ cathode interlayer. (e) Porous LSM cathode current collector. Cell fabrication procedure is briefly described in what follows. NiO and YSZ powders obtained from commercial vendors were mixed in the desired ratio, 70 wt.% NiO + 30 wt.% YSZ, to which carbon powder was added. The amount of carbon added was based on the desired porosity. Pellets of approximately 3 cm diameter were die-pressed. A thin layer of NiO + YSZ, which is the anode interlayer, was drop-coated on one surface of the disc. After drying, a thin layer of YSZ electrolyte was drop-coated on the same surface. The resulting pellets were sintered in air at 1400 °C for 2 h. This procedure leads to the formation of a fully dense YSZ electrolyte layer, supported on NiO + YSZ anode interlayer/NiO + YSZ support. After sintering the disc is about 2.6 cm in diameter. A thin layer of LSM + YSZ containing ∼50 wt.% LSM + ∼50 wt.% YSZ cathode interlayer was painted on the YSZ layer. The cell was then fired at 1200 °C for 2 h. After firing a layer of LSM cathode current collector was applied. The area of the cathode was 2 cm^2, which was used as the basis for the current density calculation. The cell was then heated to 1100 °C to ensure that the cathode was well formed, while still maintaining a significant level of porosity. This completes cell fabrication. One parameter was varied at a time to study the effect of a given parameter. The parameters varied were: (1) electrolyte

thickness, varied between ∼4 and ∼20 μm. (2) Anode support thickness, varied between 0.5 and 2.45 mm. (3) Anode support porosity, varied between 32 and 76% and (4) cathode interlayer thickness, varied between 6 and 105 μm. Parameters of standard cells, against which performance of other cells was compared, were as follows: YSZ electrolyte thickness ∼8 μm, anode support thickness ∼1 mm, anode support porosity ∼48%, cathode interlayer thickness ∼20 μm, anode interlayer thickness ∼20 μm, and cathode current collector thickness ∼50 μm. In the present work, anode interlayer thickness and cathode current collector thickness were not varied. Also, the relative proportions of constituents in a given layer were not varied, and neither were microstructures and porosities (with the exception of the anode support, whose porosity was varied over a range as stated above).

2.2. Cell testing

For testing, a typical cell was mounted in a test fixture, a schematic of which is shown in Fig. 1. Silver wires were connected to silver meshes pressed against the LSM cathode current collector and the Ni + YSZ anode support, respectively. Two sets of silver leads, one on each side, were used for current collection and voltage measurement. Care was taken to ensure that on a given side, the two silver leads were welded on the mesh at the same point. The cell was heated to 800 °C while circulating a mixture of 10% H_2 + 90% N_2 on the anode side, and air on the cathode side. NiO from the anode was reduced to Ni in a few minutes to an hour, leading to the formation of additional porosity. Subsequently, humidified hydrogen was circulated past the anode, and air was circulated past the cathode. The hydrogen and air flow rates were 300 and 550 ml min^{-1}, respectively. Voltage versus current density polarization curves were obtained over a range of temperatures between 600 and 800 °C.

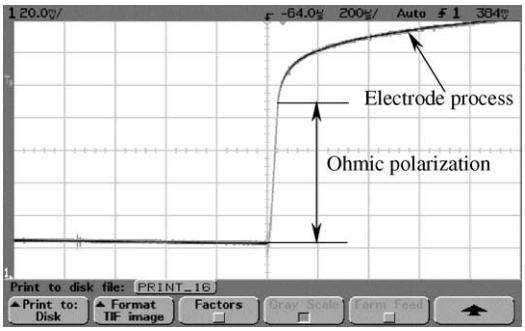

Fig. 2. An oscilloscope trace illustrating the time dependence of the electric potential before and after current interruption.

2.3. Measurement of ohmic contribution

Current interruption technique was used to obtain the ohmic contribution. The equipment used includes a Solartron S11287 Electrochemical Interface and Agilent 54622A Digital Oscilloscope. Fig. 2 shows a typical voltage versus time trace immediately following current interruption. The sharp change in voltage corresponds to the ohmic loss, and the slow change corresponds to non-ohmic polarization losses (activation and concentration). Before the current was interrupted, care was taken to ensure the attainment of steady state. In a few cases, current interruption tests were conducted by varying the applied current, which was varied between 0.5 and 2 A. Fig. 3 shows the measured voltage drop as a function of imposed current density. A linear relation between voltage change and current suggests that the ohmic portion was accurately captured in the experiments. Alternatively, these experiments suggest that the time constants for non-ohmic polarizations were considerably longer than the timescale of the current interruption experiment.

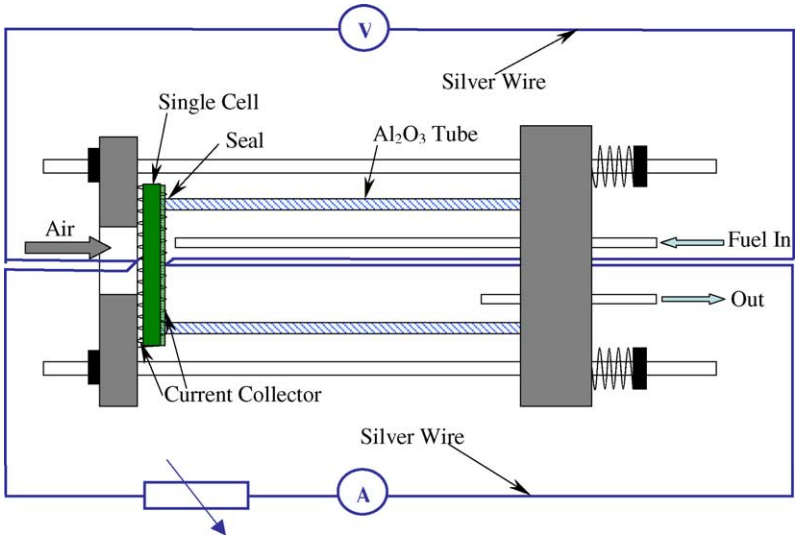

Fig. 1. A schematic of the single cell testing apparatus used.

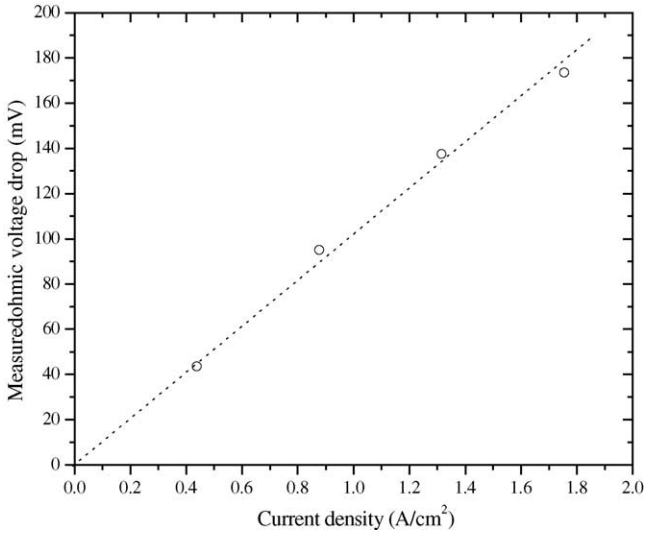

Fig. 3. Measured ohmic voltage loss as a function of current density on a standard cell at 800 °C.

2.4. Microstructure characterization

After testing, some of the cells were fractured and cross sections were examined under a scanning electron microscope (SEM). The fractured pieces of some of the samples were vacuum-impregnated with an epoxy. After hardening the epoxy, the samples were polished down to a 1 μm finish. The porosity in the anode interlayer, anode support, cathode interlayer and cathode current collector layer was determined by quantitative stereology using the systematic point count procedure [4].

3. Results

3.1. Microstructure of single cells

Fig. 4 shows an SEM micrograph of the fracture surface of a typical cell after testing. Note that the electrolyte layer is essentially fully dense, as evidenced by the existence of only a few isolated pores. The porous regions of the cathode interlayer, the anode interlayer and the anode support structure are clearly visible in the figure. Although not visible in the micrograph, separate measurements have shown that on the anode side, Ni, YSZ and porosity form contiguous, three-dimensional interpenetrating networks, and there is a considerable amount of Ni–YSZ-pore three-phase boundary (TPB) present. The existence of TPB is critical, as these are the physical locations where the electrochemical reaction of hydrogen oxidation occurs. Similar interpenetrating networks exist between LSM–YSZ-pores with TPB in the cathode interlayer, where the electrochemical reaction of oxygen reduction occurs. Recent work has shown a profound effect of TPB length in composite cathodes on cell performance [5].

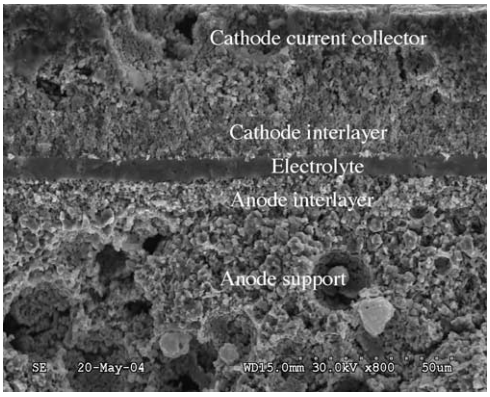

Fig. 4. An SEM micrograph of a typical cell.

3.2. Single cell test results

Fig. 5 shows the performance of a standard cell tested at 600, 700 and 800 °C. The maximum power density (MPD) is ∼0.2 W cm^{-2} at 600 °C, ∼0.6 W cm^{-2} at 700 °C and ∼1.2 W cm^{-2} at 800 °C. Fig. 6 shows the measured voltage versus current density traces at 800 °C for cells in which the only parameter varied was the YSZ electrolyte thickness, which was varied between 4 and 20 μm, all other parameters having been fixed at their standard values. As shown in Fig. 6, cells with 8 and 15 μm electrolyte thickness exhibit MPD of about 1.2 W cm^{-2}, while that with 20 μm exhibits an MPD of 1 W cm^{-2}. The cell with a 4 μm electrolyte thickness exhibits MPD of ∼1.1 W cm^{-2}. Fig. 7 shows the performance curves for the same cells at 700 °C. The cell with an 8 μm electrolyte thickness exhibits MPD of ∼0.6 W cm^{-2}, which is much lower than at 800 °C. This is due to the low ionic conductivity of electrolyte material and lower rate of electrochemical reactions at lower temperatures.

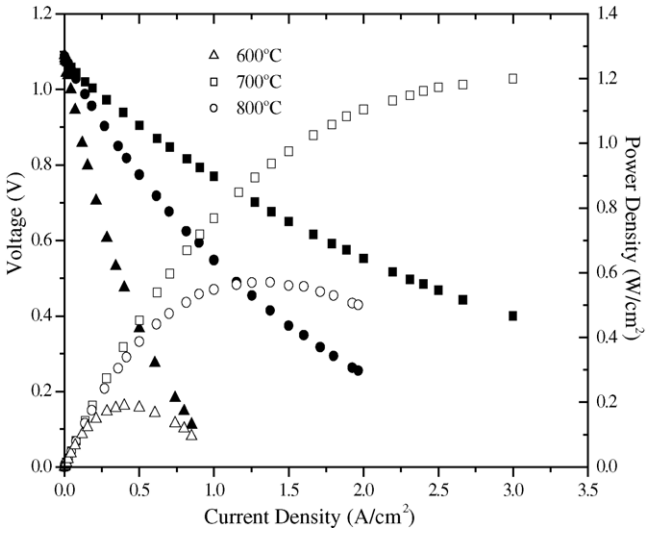

Fig. 5. Voltage and power density vs. current density plots for a standard cell at 600, 700 and 800 °C.

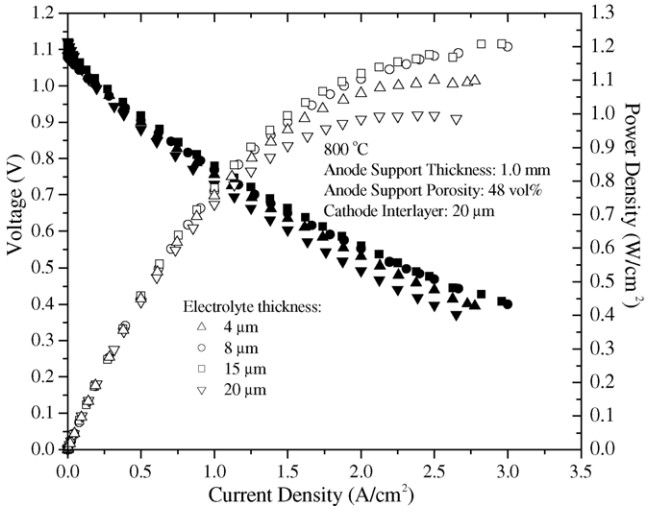

Fig. 6. Voltage and power density vs. current density plots at 800 °C for cells with different electrolyte thicknesses.

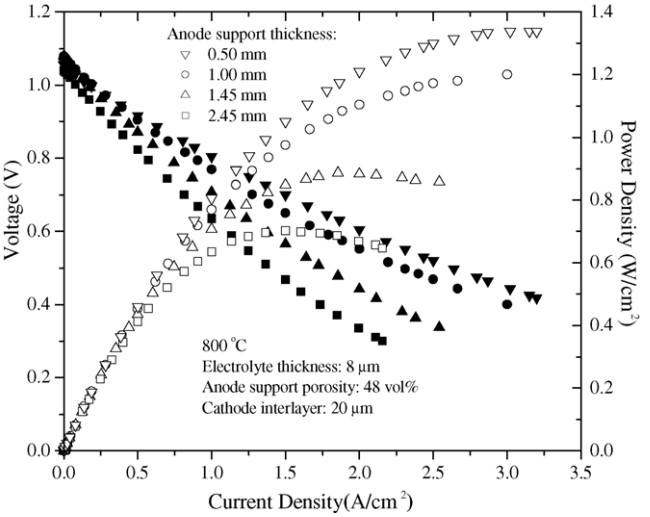

Fig. 8. Voltage and power density vs. current density plots at 800 °C for cells with different anode thicknesses.

Fig. 8 shows the results of cell tests at 800 °C wherein the anode support thickness was varied between 0.5 and 2.45 mm, all other parameters fixed at the standard values. Note that the MPD varies between ∼0.7 W cm^{-2} for anode support thickness of 2.45 mm to ∼1.35 W cm^{-2} for anode support thickness of 0.5 mm showing a profound effect of anode support thickness on performance. Fig. 9 shows the results of cell tests wherein the anode support porosity was varied between 32 and 76%, all other parameters maintained at the standard values. Note that the MPD for a cell with anode support porosity of 32% is only ∼0.72 W cm^{-2}, while that for a cell with anode support porosity of 57% is ∼1.55 W cm^{-2}. This shows the profound effect of anode support porosity on cell performance. The MPD for the cell with anode support porosity of 76% was about 1.5 W cm^{-2}. The lower performance of this cell despite higher porosity of the anode support is due to the fact that the open circuit voltage (OCV) of this cell was lower, indicating that there was presumably leakage through the electrolyte. Fig. 10 shows the results of cell tests with all parameters maintained at the standard values, with only the cathode interlayer thickness varied between ∼6 and ∼105 μm. Note that the MPD is the highest for cathode interlayer thickness of 20 μm, and is lower for cells with cathode interlayer thicknesses either smaller or larger than 20 μm.

Fig. 11 shows the results of cell tests with optimized parameters: anode support thickness = 0.5 mm, anode interlayer thickness = 20 μm, anode support porosity = 57%, electrolyte thickness = 8 μm, cathode interlayer = 20 μm and cathode current collector = 50 μm. In the present work, anode interlayer thickness and cathode current collector thickness were not varied. The MPD is ∼1.8 W cm^{-2} at 800 °C,

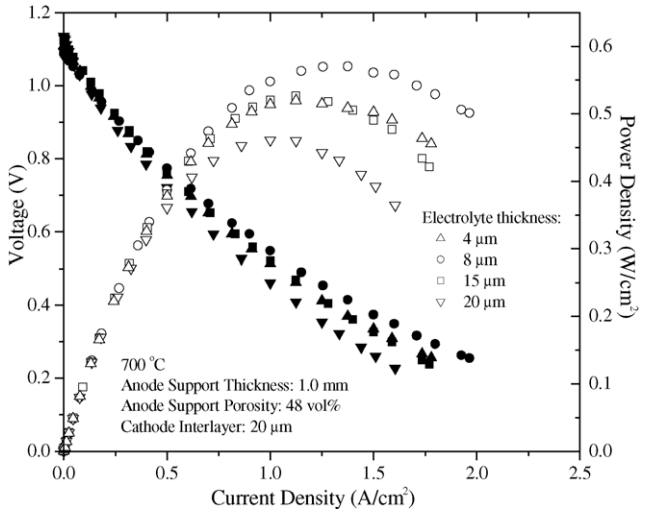

Fig. 7. Voltage and power density vs. current density plots at 700 °C for cells with different electrolyte thicknesses.

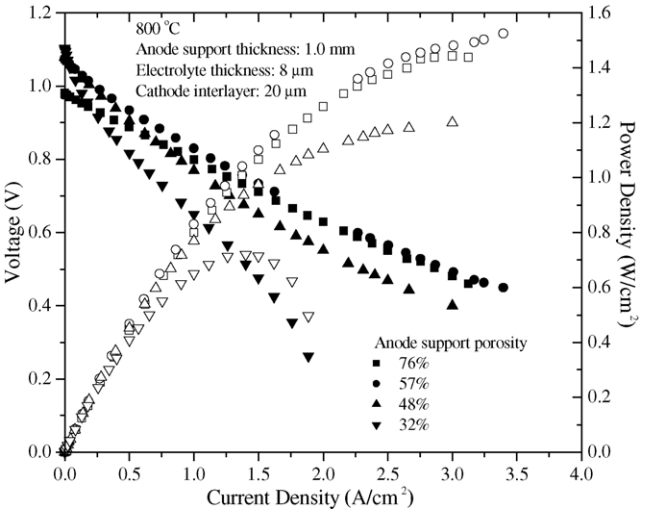

Fig. 9. Voltage and power density vs. current density for cells with anode porosity varied between 32 and 76%. The OCV for the cell with 76% anode support porosity is lower than the theoretical value, indicating that the YSZ electrolyte film was not gas-tight.

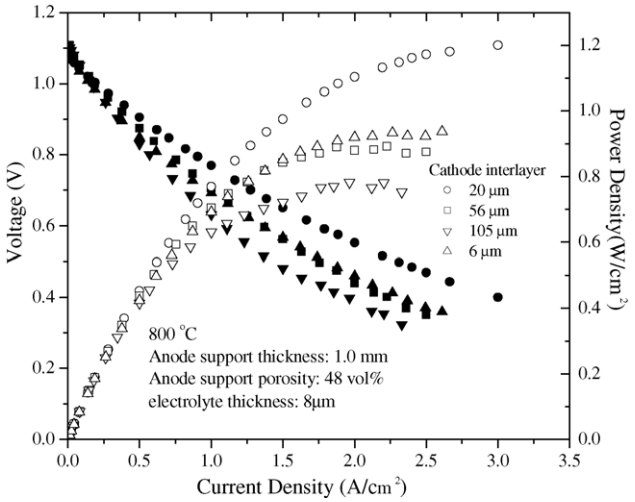

Fig. 10. Voltage and power density vs. current density for cells with cathode interlayer thickness varied between ∼6 and ∼105 μm.

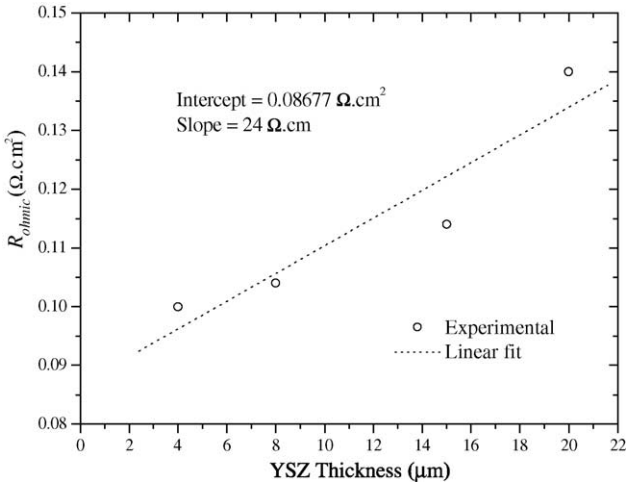

Fig. 12. Measured ohmic area specific resistance (ASR) as a function of YSZ electrolyte thickness at 800 °C.

∼0.8 W cm^{-2} at 700 °C, and ∼0.4 W cm^{-2} at 600 °C. The results demonstrate that the cell with the optimized parameters exhibits the highest performance.

3.3. Area specific ohmic resistance (ASR)

The results of area specific ohmic resistance (ASR) measured by current interruption on cells as a function of electrolyte thickness, anode support thickness, anode support porosity and cathode interlayer thickness are given in Table 1. As seen in Table 1, note that the ASR increases with increasing electrolyte thickness, increasing anode support thickness, and increasing cathode interlayer thickness. However, the ASR decreases with increasing anode support porosity. Fig. 12 is a plot of ASR at 800 °C as a function of electrolyte thickness. The slope of the plot is ∼24 Ω cm and the intercept is ∼0.087 Ω cm^2. Fig. 13 is a similar plot for cell tests conducted at 700 °C, with slope equal to ∼63 Ω cm and intercept ∼0.138 Ω cm^2. Fig. 14 is a plot of ASR at 800 °C as a function of anode support thickness. The corresponding slope and intercept are respectively, 0.24 Ω cm and 0.084 Ω cm^2. Fig. 15 is a plot of ASR at 800 °C as a function of cathode interlayer thickness. The corresponding slope and intercept are respectively, 3.922 Ω cm and 0.095 Ω cm^2. Finally, Fig. 16 is a plot of the measured ASR at 800 °C as a function of anode support porosity.

The ASR measured by current interruption on standard cells as a function of temperature is given in Table 2. The ASR increases from 0.104 to 0.19 (cm^2 with the decrease of temperature from 800 to 700 °C. The ASR for the cell with optimized parameters is also given in Table 2. Note that for the optimized cell, the ASR increases from 0.085 Ω cm^2 at 800 °C to 0.15 Ω cm^2 at 700 °C.

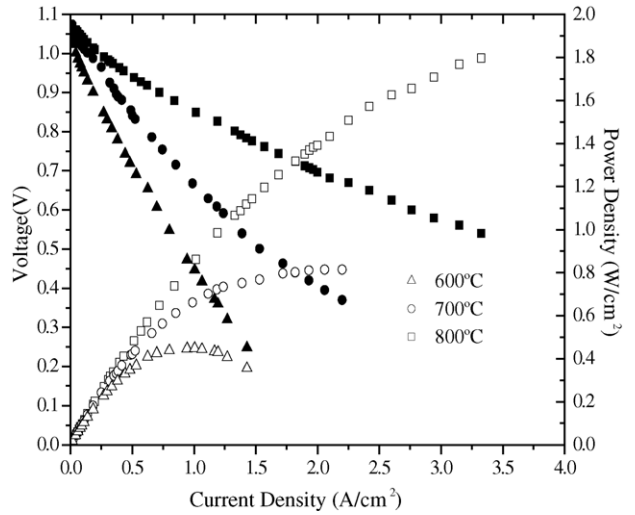

Fig. 11. Voltage and power density vs. current density for an optimized cell over a range of temperatures between 600 and 800 °C.

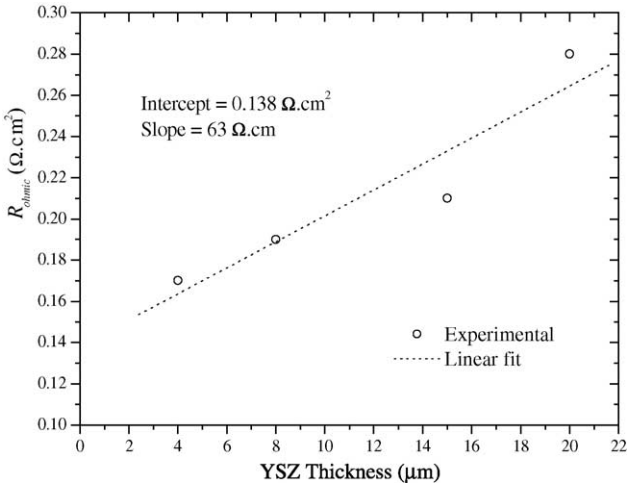

Fig. 13. Measured ohmic area specific resistance (ASR) as a function of YSZ electrolyte thickness at 700 °C.

Table 1
Ohmic resistance of cells measured by current interruption

Anode support thickness 1 mm, anode interlayer thickness 20 μm, electrolyte thickness 8 μm, anode support porosity 48%, cathode interlayer thickness 20 μm, cathode current collector thickness 50 μm				
Electrolyte thickness (μm)	4	8	15	20
Ohmic resistance (ohm cm^2)	0.1	0.104	0.114	0.14
Ohmic resistance[a] (ohm cm^2)	0.17	0.19	0.27	0.28
Anode support porosity 48%, anode interlayer thickness 20 μm, electrolyte thickness 8 μm, cathode interlayer thickness 20 μm, cathode current collector thickness 50 μm				
Anode support thickness (mm)	0.5	1.0	1.5	2.45
Ohmic resistance (ohm cm^2)	0.095	0.104	0.13	0.14
Anode support thickness 1 mm, anode interlayer thickness 20 μm, electrolyte thickness 8 μm, cathode interlayer thickness 20 μm, cathode current collector thickness 50 μm				
Anode support porosity (%)	32	48	57	76
Ohmic resistance (ohm cm^2)	0.156	0.104	0.09	0.074
Anode support thickness 1 mm, anode support porosity 48%, anode interlayer thickness 20 μm, electrolyte thickness 8 μm, cathode current collector thickness 50 μm				
Cathode interlayer thickness (μm)	6	20	56	105
Ohmic resistance (ohm cm^2)	0.095	0.104	0.12	0.135

[a] The ohmic resistance measured at 700 °C. All other measurements at 800 °C.

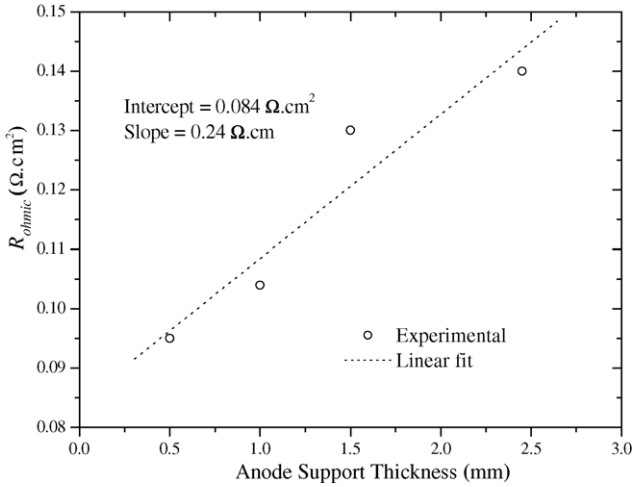

Fig. 14. Measured ohmic area specific resistance (ASR) as a function of anode support thickness at 800 °C.

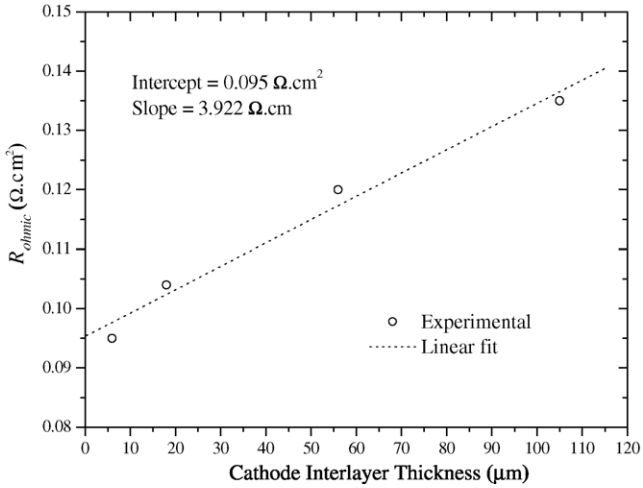

Fig. 15. Measured ohmic area specific resistance (ASR) as a function of cathode interlayer thickness at 800 °C.

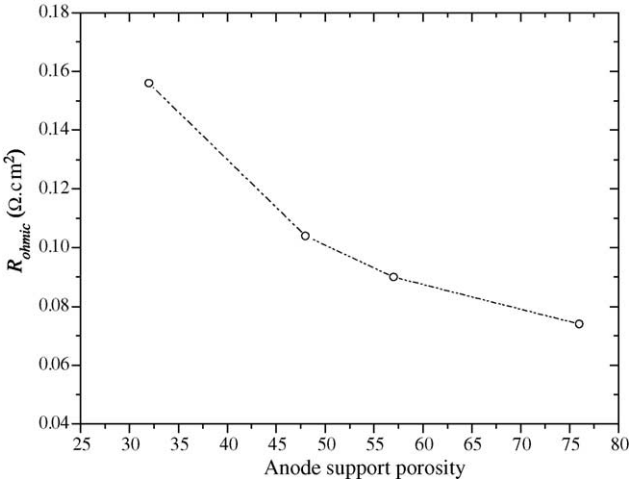

Fig. 16. Measured ohmic area specific resistance (ASR) as a function of anode support porosity at 800 °C.

Table 2
Ohmic resistance (by current interruption) as a function of temperature for standard and optimized cells

Temperature (°C)	700	800
Ohmic ASR of standard cell (ohm cm^2)	0.19	0.104
Ohmic ASR of optimized cell (ohm cm^2)	0.15	0.085

3.4. Measurement of porosity

Measured porosity levels using quantitative stereology were ∼26% for the cathode interlayer, ∼45% for the cathode current collector, and ∼23% for the anode interlayer.

4. Discussion

4.1. Effect of various parameters on the ohmic area specific resistance (ASR)

For a given set of materials, compositions and microstructures, the ASR is a function of the thicknesses of the electrolyte, the two electrodes, and the possible interfacial or contact resistances. In the present work, each cell comprised of five distinct layers; porous Ni + YSZ anode support, porous Ni + YSZ anode interlayer, dense YSZ electrolyte, porous LSM + YSZ cathode interlayer, and porous LSM current collector. Thus, the ASR, R_i, may be given as

$$R_i = \rho_e^{ionic} l_e + \rho_{c(1)}^{elect} l_{c(1)} + \rho_{c(2)}^{elect} l_{c(2)} + \rho_{a(1)}^{elect} l_{a(1)} + \rho_{a(2)}^{elect} l_{a(2)} + R_{contact} \quad (2)$$

where ρ_e^{ionic} and l_e are respectively, the electrolyte ionic resistivity and thickness, $\rho_{c(1)}^{elect}$ and $l_{c(1)}$ are respectively, the cathode current collector electronic resistivity and thickness, $\rho_{c(2)}^{elect}$ and $l_{c(2)}$ are respectively, cathode interlayer electronic resistivity and thickness, $\rho_{a(1)}^{elect}$ and $l_{a(1)}$ are respectively, anode support electronic resistivity and thickness, $\rho_{a(2)}^{elect}$ and $l_{a(2)}$ are respectively, anode interlayer electronic resistivity and thickness, and $R_{contact}$ is some contact resistance, representative of resistance associated with interfaces. A schematic of a typical cell with various regions labeled is shown in Fig. 17.

In cases wherein the only parameter varied is the thickness of one of the layers, the thickness dependence of resistance can be unequivocally attributed to the resistivity of that layer. For example, in cells in which the only parameter varied was the YSZ electrolyte thickness, the dependence of ASR on thickness can be uniquely related to the resistivity of dense YSZ. It is expected that cells with the thinnest electrolyte (∼4 μm) should exhibit the highest performance. The observation that the cell with the ∼4 μm electrolyte does not exhibit the highest MPD as shown in Fig. 6 simply implies that: (1) the cells were not identical in all other respects, despite the intent. For example, there might have been small (unintended) differences in the thicknesses and/or microstructures of the other layers. (2) The electrolyte ohmic contribution is not the overriding factor at these low electrolyte thicknesses.

Since the only parameter varied is the electrolyte thickness, the Eq. (2) can be written as

$$R_i = \rho_e^{ionic} l_e + R_{const} \quad (3)$$

where R_{const} is the contribution to ASR from sources other than the electrolyte. Thus, a plot of the measured ASR versus the electrolyte thickness, l_e, should be linear with the slope equal to the electrolyte ionic resistivity, ρ_e^{ionic} and intercept R_{const}. A plot of the ohmic area specific resistance (ASR) at 800 °C measured by current interruption versus l_e is shown in Fig. 12 with the slope ∼24 Ω cm, which is in good agreement with the reported value of the resistivity of YSZ electrolyte (of typical grain size on the order of a few microns) of 22.3 Ω cm at 800 °C [6]. Note, however, that the intercept is nonzero (0.087 Ω cm^2), indicating that there are other sources of substantial ohmic contribution. Fig. 13 shows a similar plot of the measured ASR by current interruption versus l_e at 700 °C. The measured electrolyte resistivity from the plot is ∼63 Ω cm and the corresponding intercept is ∼0.138 Ω cm^2, showing that a substantial contribution to the ohmic contribution from sources other than the electrolyte is also present at 700 °C.

Fig. 14 is a plot of the ASR as a function of anode support thickness at 800 °C. Since the only parameter varied was the anode support thickness, the ASR as a function of anode support thickness is given by

$$R_i = \rho_{a(1)}^{elect} l_{a(1)} + R'_{const} \quad (4)$$

where the slope is the electronic resistivity of the anode support, $\rho_{a(1)}^{elect}$, and the intercept is R'_{const}, which is the ohmic part due to sources other than the anode support. From Fig. 14, the estimated value of $\rho_{a(1)}^{elect}$ is ∼0.24 Ω cm and the intercept,

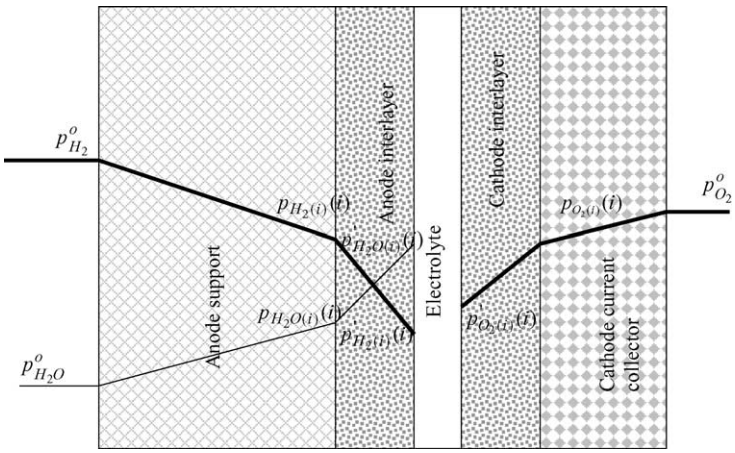

Fig. 17. A schematic diagram of an anode-supported cell comprising five distinct layers, and variation of partial pressures of the various gaseous species.

Table 3
Calculated electrolyte ohmic contribution and measured total ohmic contribution (by current interruption) at 800 °C

YSZ thickness (μm)	$R_{electrolyte}$ (calculated)[a] ($\Omega\,cm^2$)	R_{ohmic} (measured) ($\Omega\,cm^2$)	ΔR_{ohmic} ($\Omega\,cm^2$)
4	0.0096	0.10	0.0904
8	0.0192	0.104	0.0848
15	0.036	0.114	0.078
20	0.048	0.140	0.092

[a] Electrolyte resistivity = 24 Ω cm.

R'_{const} is ∼0.084 Ω cm^2. In the anode support, the volume fraction of Ni is ∼35%, the remainder being porosity (essentially infinite resistivity) and YSZ (also of very high resistivity, in comparison to Ni). That is, for all practical purposes, the volume fraction of conductive phase (Ni) is ∼35%. It is known that at relatively high volume fractions of insulating phases, the net conductivity can be far below that of the conductive phase corrected for porosity through a simple linear relationship, provided the inter particle contact is poor. For example, it has been found that a plot of relative conductivity, $\sigma(V_v)/\sigma_o$, versus relative density, $\zeta(V_v)/\zeta_o$ where σ_o is the conductivity of a fully dense material, $\sigma(V_v)$ is the conductivity of a material with V_v volume fraction porosity, ζ_o is the density of fully dense material, and $\zeta(V_v)$ is the density of a material with porosity V_v is often approximately linear and extrapolation intersects the $\zeta(V_v)/\zeta$ axis at ∼0.45–∼0.6. That is, the $\sigma(V_v)/\sigma_o$ almost approaches zero for $V_v \geq 0.45$ [7–9]. That is, often the contiguity between conductive particles is very poor. In light of this, even though σ_o for Ni at 800 °C is very high (∼7.94×10^4 S cm^{-1}), it is not surprising that the estimated $\sigma(V_v)$ (for $V_v \sim 0.65$) is only 1/0.24 or ∼4.4 S cm^{-1}.

Fig. 15 is a plot of ASR as a function of cathode interlayer thickness at 800 °C. Since the only parameter varied was the cathode interlayer thickness, the ASR as a function of cathode interlayer thickness is given by

$$R_i = \rho^{elect}_{c(2)} l_{c(2)} + R''_{const} \quad (5)$$

where the slope is essentially the electronic resistivity of the cathode interlayer, $\rho^{elect}_{c(2)}$, and the intercept is R''_{const}, which is the ohmic contribution from sources other than the cathode interlayer. As seen in Fig. 15, the slope, $\rho^{elect}_{c(2)}$ is estimated to be 3.922 Ω cm and the intercept, R''_{const} is ∼0.095 Ω cm^2. The electronic resistivity of fully dense LSM at 800 °C is ∼2×10^{-2} Ω cm. The fact that the estimated $\rho^{elect}_{c(2)}$ from the slope is considerably higher (lower conductivity) is consistent with the rather high volume fraction of the insulating phase, namely porosity + YSZ ($V_v \sim 0.65$), such that connectivity (particle to particle contact) is poor.

Independent measurement of cell ASR as a function of relative thicknesses thus has facilitated the estimation of the various resistivities, namely, ρ^{ionic}_e, $\rho^{elect}_{a(1)}$, and $\rho^{elect}_{c(2)}$. In the standard cells, the l_e, $l_{a(1)}$ and $l_{c(2)}$ were respectively, 8 μm, 1 mm, and 20 μm. Thus, for the standard cells, the estimated ohmic ASR at 800 °C is

$$R_i = 24 \times 8 \times 10^{-4} + 0.24 \times 10^{-1} + 3.922 \times 20 \times 10^{-4} + R'''_{const} = 0.051 + R'''_{const}\ \Omega\,cm^2$$

wherein

$$R'''_{const} = \rho^{elect}_{a(2)} l_{a(2)} + \rho^{elect}_{c(1)} l_{c(1)} + R_{contact}$$

The experimentally measured ASR by current interruption is ∼0.104 Ω cm^2. Thus, the estimated value of R'''_{const} is 0.104 − 0.051 = 0.053 Ω cm^2. That is, approximately half of the ohmic ASR at 800 °C of the standard cells used in this work is attributed to resistances of the Ni + YSZ anode interlayer, LSM cathode current collector, and any possible contact resistances. Tables 3 and 4, respectively, list the measured cell ohmic ASR at 800 and 700 °C, along with calculated electrolyte contribution for electrolyte thickness ranging between 4 and 20 μm. Note that even for an electrolyte thickness of 20 μm and at 700 °C, its ohmic contribution to the ASR is lower than that due to other sources. For a 8 μm electrolyte thickness, the electrolyte contribution to the ohmic ASR at 800 °C is ∼0.0192 Ω cm^2, which corresponds to ∼19% of the total ohmic ASR. At 700 °C, the electrolyte contribution is ∼0.0504 Ω cm^2, which is ∼27% of the total ohmic ASR. This shows that even at temperatures as low as 700 °C, the ohmic contribution of a thin (∼8 μm) YSZ electrolyte is rather small, and that YSZ is a satisfactory electrolyte. Also, it is seen that there is no need to lower the electrolyte thickness much below about 8 μm, since the electrolyte contribution to the overall ASR is rather modest. That is, although an electrolyte material exhibiting

Table 4
Calculated electrolyte contribution and measured total ohmic contribution (by current interruption) at 700 °C

YSZ thickness (μm)	$R_{electrolyte}$ (calculated)[a] ($\Omega\,cm^2$)	R_{ohmic} (measured) ($\Omega\,cm^2$)	ΔR_{ohmic} ($\Omega\,cm^2$)
4	0.0252	0.17	0.145
8	0.0504	0.19	0.14
15	0.0945	0.21	0.12
20	0.126	0.28	0.154

[a] Electrolyte resistivity = 63 Ω cm.

higher ionic conductivity than YSZ is preferred, it is not an absolute necessity for intermediate temperature SOFC operating at temperatures ≥700 °C. This also means that conventional, thick film processing methods capable of producing supported YSZ membranes of a thickness on the order of a few microns, are satisfactory for the fabrication of electrolyte films of SOFC. Further work will be required to determine $\rho_{a(2)}^{elect}$ and $\rho_{c(1)}^{elect}$ by varying respectively, the anode interlayer thickness and the cathode current collector thickness. If this is done, it will allow the estimation of the contact resistance, $R_{contact}$.

Fig. 16 shows the dependence of ohmic ASR as a function of anode support porosity. Over the range of porosities investigated, the ASR decreases with increasing porosity—from 0.156 Ω cm^2 at 32% porosity to 0.074 Ω cm^2 at 76% porosity. This behavior appears unreasonable, since it would be expected with increase in porosity (decrease in volume fraction of Ni), the net contribution to the ohmic ASR should increase. The volume fraction of Ni in the sample containing 32% porosity was ∼0.47, and that containing 76% porosity was ∼0.16. The resistivity of Ni at 800 °C is 1.26×10^{-5} Ω cm or conductivity of 7.94×10^4 S cm^{-1}. If a simple linear relationship can be assumed between conductivity and volume fraction of Ni, namely $\sigma(V_{Ni}) \approx \sigma_o V_{Ni}$, the expected contributions to ASR for a 1 mm thick anode support are 2.68×10^{-6} Ω cm^2 for 32% porosity and 7.87×10^{-6} Ω cm^2 for 76% porosity. Clearly, these are rather small values compared to the experimental measurements, which are respectively, 0.156 and 0.074 Ω cm^2, or the measured ASRs are greater by factors of $0.156/(2.68 \times 10^{-6}) \sim 58{,}210$ and $0.074/(7.87 \times 10^{-6}) \sim 9400$), respectively. This means that there must be other factors indirectly dependent on porosity, which exhibit greater effect on the overall conductivity of anode support. The most likely one is the nature of contiguity—namely the inter particle contact geometry. An approximate order of magnitude effect of the geometry of contact can be determined by making simple calculations based on an assumed geometry. If nickel particles are assumed to be spherical of radius r and if the inter particle neck radius is r_o, it can be shown that the effective resistivity of a body comprising spheres is given by

$$\rho_{eff} \approx \frac{\rho_{Ni}}{2\sqrt{1-\lambda^2}} \ln\left\{\frac{1+\sqrt{1-\lambda^2}}{1-\sqrt{1-\lambda^2}}\right\} \quad (6)$$

where $\lambda = r_o/r$, is a measure of the relative neck size—or alternatively, how good the contact is between particles. Note that as $\lambda \to 0$, the effective resistivity of the body approaches infinity, showing the profound effect of contact geometry. Presumably, the microstructure in the porous electrodes must be such that in the sample with 76% porosity, even though the volume fraction of Ni is low (∼0.16), the contiguity must be greater than the sample with larger Ni content. Unfortunately, in the absence of detailed quantitative microstructural characterization of the anode, this question remains unanswered at the present time.

4.2. Concentration and activation polarizations: comparison of experimental results on cell tests with an analytical model

Fig. 17 shows a schematic of the cross section of a cell, along with schematic variations in the partial pressures of various gaseous species. In terms of the various parameters related to transport and electrode reactions, it is possible to describe the voltage versus current density relationship mathematically. Several models have been proposed, with varying degrees of complexity and requiring a number of different parameters [1,10,11]. In this work, one of the simplest models requiring a relatively small number of parameters is used. The partial pressures of hydrogen in the fuel (outside of the anode) and of oxygen in the oxidant (outside of the cathode) are given respectively, by $p^o_{H_2}$ and $p^o_{O_2}$. The fuel is usually humidified. The partial pressure of H_2O in the fuel, just outside the anode, is $p^o_{H_2O}$. In the present work, the values of hydrogen and H_2O partial pressures were respectively, $p^o_{H_2} \approx 0.97$ atm and $p^o_{H_2O} \approx 0.03$ atm. The partial pressures of hydrogen and H_2O at the anode support/anode interlayer interface corresponding to a current density of i are given respectively, by $p_{H_2(i)}(i)$ and $p_{H_2O(i)}(i)$, and that of oxygen at the cathode current collector/cathode interlayer interface is given by $p_{O_2(i)}(i)$. Finally, partial pressures of hydrogen and H_2O at the anode interlayer/electrolyte interface are given respectively, by $p'_{H_2(i)}(i)$ and $p'_{H_2O(i)}(i)$, and that of oxygen at the cathode interlayer/electrolyte interface is given by $p'_{O_2(i)}(i)$. In what follows, it is assumed that the flow rates of fuel and oxidant are sufficiently fast such that $p^o_{H_2}$ and $p^o_{O_2}$ are constant, independent of current density (that is, both fuel and oxidant utilization are negligible) [12]. The partial pressures of hydrogen and oxygen in the electrodes, however, are functions of current density. It can be shown that that anodic concentration polarization with an H_2–H_2O gas mixture as fuel is given by [1]

$$\eta_{a,con} = -\frac{RT}{2F} \ln\left(\frac{p'_{H_2(i)}(i)\, p^o_{H_2O}}{p^o_{H_2}\, p'_{H_2O(i)}(i)}\right) \quad (7)$$

where R is the ideal gas constant and F is the Faraday constant. Local equilibrium is assumed, which for anode means that locally, p_{H_2}, p_{H_2O}, and p_{O_2} are related to each other via the equilibrium

$$H_2 + \tfrac{1}{2}O_2 \rightarrow H_2O$$

In what follows, it will be assumed that gaseous transport through the porous electrodes can be adequately described by binary diffusion and that there is negligible contribution of viscous flow. The microstructure within a given region, e.g. the anode support or the anode interlayer, is expected to be uniform. Under these conditions, the partial pressures of H_2 and H_2O within a given region are expected to vary linearly with position, as shown in Fig. 17. It is to be noted, however, that the partial pressure of oxygen at the anode, which is much lower than the partial pressures of hydrogen

and H_2O, i.e. $p_{O_2(a)} \ll p_{H_2}$, p_{H_2O}, does not vary linearly, but is governed by the above H_2/H_2O equilibrium. It is also to be mentioned that the variation of p_{H_2} and p_{H_2O} in the anode interlayer, especially close to the electrolyte, is not expected to be linear. This is because within this layer, individual fluxes in the gas phase are not conserved, even though $p_{H_2} + p_{H_2O}$ continues to remain fixed. This aspect is ignored here.

The effective anode support and anode interlayer diffusivities are respectively, $D^{\text{eff}(1)}_{H_2-H_2O}$ and $D^{\text{eff}(2)}_{H_2-H_2O}$, wherein it is assumed that the effective diffusivities are proportional to the H_2–H_2O binary diffusivity ($D_{H_2-H_2O}$), volume fraction porosity, and inversely proportional to tortuosity factor. Since other effects, such as Knudsen diffusion are likely present, and the exact nature of tortuosity is unclear, in the above description the tortuosity factor is a merely phenomenological fitting parameter. In steady state, under the assumptions made, the partial pressures of hydrogen and H_2O at the anode interlayer/electrolyte interface as a function of current density are given respectively, by

$$p'_{H_2(i)}(i) = \frac{l_{a(2)}}{D^{\text{eff}(2)}_{H_2-H_2O}}\left[\frac{p^o_{H_2} D^{\text{eff}(2)}_{H_2-H_2O}}{l_{a(2)}} - \frac{iRTl_{a(1)}}{2FD^{\text{eff}(1)}_{H_2-H_2O}} \times \left(\frac{D^{\text{eff}(2)}_{H_2-H_2O}}{l_{a(2)}} + \frac{D^{\text{eff}(1)}_{H_2-H_2O}}{l_{a(1)}}\right)\right] \quad (8)$$

and

$$p'_{H_2O(i)}(i) = \frac{l_{a(2)}}{D^{\text{eff}(2)}_{H_2-H_2O}}\left[\frac{p^o_{H_2O} D^{\text{eff}(2)}_{H_2-H_2O}}{l_{a(2)}} + \frac{iRTl_{a(1)}}{2FD^{\text{eff}(1)}_{H_2-H_2O}} \times \left(\frac{D^{\text{eff}(2)}_{H_2-H_2O}}{l_{a(2)}} + \frac{D^{\text{eff}(1)}_{H_2-H_2O}}{l_{a(1)}}\right)\right] \quad (9)$$

The maximum possible current density corresponds to the lowest possible partial pressure of hydrogen at the anode interlayer/electrolyte interface, which is zero (although it can never be exactly zero). Thus, setting Eq. (8) equal to zero gives the anode limiting current density, given by

$$i_{as} = \frac{2Fp^o_{H_2} D^{\text{eff}(1)}_{H_2-H_2O} D^{\text{eff}(2)}_{H_2-H_2O}}{RTl_{a(1)}l_{a(2)}(D^{\text{eff}(1)}_{H_2-H_2O}/l_{a(1)} + D^{\text{eff}(2)}_{H_2-H_2O}/l_{a(2)})} \quad (10)$$

If all of the requisite parameters are known, for a given current density, i, the $p'_{H_2(i)}(i)$ and $p'_{H_2O(i)}(i)$ can be estimated from Eqs. (8) and (9), respectively, and the anodic concentration polarization can be calculated using Eq. (7).

Concentration polarization at the cathode can be similarly examined. The oxidant is typically air, a mixture of O_2 and N_2.

A schematic of a porous cathode, along with the spatial variation of partial pressure of oxygen is also shown in Fig. 17. For an anode-supported cell with a small cathode thickness, the oxygen partial pressure at the interface of current collector and cathode interlayer can be given by [13]

$$p_{O_2(i)}(i) \approx p^o_{O_2} - \left(\frac{p - p^o_{O_2}}{p}\right)\left[\frac{iRTl_{c(1)}}{4FD^{\text{eff}(1)}_{O_2-N_2}}\right] \quad (11)$$

where $p^o_{O_2}$ is the oxygen partial pressure in the oxidant (air) outside of the cathode (Pa or atm), $p_{O_2(i)}(i)$ is the oxygen partial pressure at the interface between the cathode current collector and the cathode interlayer corresponding to current density i, p the total pressure, $l_{c(1)}$ the cathode current collector thickness and $D^{\text{eff}(1)}_{O_2-N_2}$ is the effective O_2–N_2 diffusivity through the cathode current collector. The oxygen flux through the current collector and cathode interlayer should be the same, i.e.

$$(p^o_{O_2} - p_{O_2(i)}(i))\left(\frac{p}{p - p^o_{O_2}}\right)\frac{D^{\text{eff}(1)}_{O_2-N_2}}{l_{c(1)}} = (p_{O_2(i)}(i) - p'_{O_2(i)}(i))\left(\frac{p}{p - p_{O_2(i)}(i)}\right)\frac{D^{\text{eff}(2)}_{O_2-N_2}}{l_{c(2)}} \quad (12)$$

where $p'_{O_2(i)}(i)$ is the oxygen partial pressure at the interface between the cathode interlayer and electrolyte, $D^{\text{eff}(2)}_{O_2-N_2}$ the effective O_2–N_2 diffusivity through the cathode interlayer, and $l_{c(2)}$ is the cathode interlayer thickness. Here also, the variation of p_{O_2} in the cathode interlayer will be nonlinear, especially close to the electrolyte/cathode interlayer interface, as the flux of O_2 is not conserved. This aspect is ignored here.

Inserting Eq. (11) into Eq. (12) and rearranging

$$p'_{O_2(i)}(i) = p^o_{O_2} - \frac{\left(\frac{iRTl_{c(1)}}{4FD^{\text{eff}(1)}_{O_2-N_2}}\right)\begin{bmatrix}(p - p^o_{O_2})(l_{c(1)}D^{\text{eff}(2)}_{O_2-N_2} \\ + l_{c(2)}D^{\text{eff}(1)}_{O_2-N_2}) \\ + \left(\frac{p-p^o_{O_2}}{p}\right)\left(\frac{iRTl_{c(1)}l_{c(2)}}{4F}\right)\end{bmatrix}}{pl_{c(1)}D^{\text{eff}(2)}_{O_2-N_2}} \quad (13)$$

The maximum possible current density is that corresponding to the lowest possible oxygen partial pressure at the interface between the cathode interlayer and the electrolyte, which is zero (although $p'_{O_2(i)}(i)$ of course can never be exactly zero). The corresponding current density, which is the cathode limiting current density, i_{cs}, is given by setting Eq. (13) to zero, and is given by

$$i_{cs} = \frac{-B + \sqrt{B^2 + 4AC}}{2A} \quad (14)$$

where the constants A–C are given by

$$A = \left(\frac{p - p^o_{O_2}}{p}\right)\frac{RTl_{c(1)}l_{c(2)}}{4F} \quad (15)$$

$$B = (p - p^o_{O_2})(l_{c(1)}D^{\text{eff}(2)}_{O_2-N_2} + l_{c(2)}D^{\text{eff}(1)}_{O_2-N_2}) \quad (16)$$

and

$$C = \frac{4Fpp^{o}_{O_2}}{RT} D^{\text{eff}(1)}_{O_2-N_2} D^{\text{eff}(2)}_{O_2-N_2} \quad (17)$$

The concentration polarization at the cathode is given by

$$\eta_{c,con} = -\frac{RT}{4F} \ln\left(\frac{p'_{O_2(i)}(i)}{p^{o}_{O_2}}\right) \quad (18)$$

Finally, the voltage versus current density, namely, $V(i)$ versus i is given by [1]

$$V(i) = E_0 - iR_i - a - b \ln i + \frac{RT}{2F} \ln\left(\frac{p'_{H_2(i)}(i)p^{o}_{H_2O}}{p^{o}_{H_2}p'_{H_2O(i)}(i)}\right) + \frac{RT}{4F} \ln\left(\frac{p'_{O_2(i)}(i)}{p^{o}_{O_2}}\right) \quad (19)$$

where it is assumed that the net activation polarization at both the cathode and anode can be described by the Tafel equation and is given by

$$\eta_{act} = a + b \ln i \quad (20)$$

Note that $p'_{H_2(i)}(i)$ and $p'_{H_2O(i)}(i)$ are functions of $D^{\text{eff}(1)}_{H_2-H_2O}$ and $D^{\text{eff}(2)}_{H_2-H_2O}$, and $p'_{O_2(i)}(i)$ is a function of $D^{\text{eff}(1)}_{O_2-N_2}$ and $D^{\text{eff}(2)}_{O_2-N_2}$, which are four of the unknown parameters. The other unknown parameters are a and b, which describe the overall activation polarization. Strictly, a and b are functions of $p'_{H_2(i)}(i)$ and $p'_{O_2(i)}(i)$, and thus themselves are functions of the current density i. This aspect is ignored here insofar as curve-fitting is concerned. However, implications of their dependence on partial pressures are discussed later. The ohmic ASR, R_i, is known from the current interruption tests. The experimental $V(i)$ versus i trace for each case was fitted using seven adjustable parameters: R_i, a, b, $D^{\text{eff}(1)}_{O_2-N_2}$, $D^{\text{eff}(2)}_{O_2-N_2}$, $D^{\text{eff}(1)}_{H_2-H_2O}$ and $D^{\text{eff}(2)}_{H_2-H_2O}$. These parameters were adjusted to obtain the best possible fit to Eq. (19). In the curve-fitting procedure, the R_i was also treated as an adjustable parameter. Fig. 18 shows a comparison with the experimental data on a cell with anode support porosity of 32% tested at 800 °C and the best fit to the data. Note that the fit is very good, except at very low current densities, where the fit diverges. This is simply the result of assuming the applicability of the Tafel equation over the entire range. However, the Tafel equation, which has a term with $\ln i$, becomes divergent as $i \to 0$. Thus, the Tafel equation is not applicable at too low a current density (lower than the exchange current density, i_o), and one must use an effective charge transfer resistance given by $R_{ct(eff)} \approx RT/zFi_o$ with the activation polarization given by $\eta_{act} \approx iR_{ct(eff)}$. This aspect was ignored in fitting the data; and hence the divergence of the fit at low current densities. That part of the fit, therefore, has been shown by a dotted line. Table 5 gives the parameters R_i, a, b, $D^{\text{eff}(1)}_{O_2-N_2}$, $D^{\text{eff}(2)}_{O_2-N_2}$, $D^{\text{eff}(1)}_{H_2-H_2O}$ and $D^{\text{eff}(2)}_{H_2-H_2O}$ corresponding to the best fits to all of the cell tests conducted.

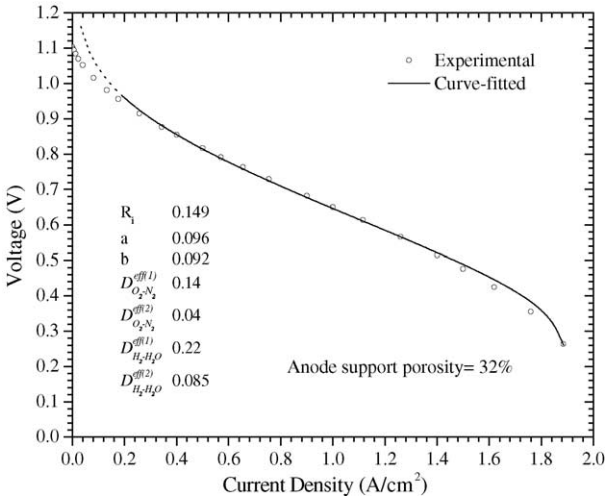

Fig. 18. Experimental voltage vs. current density plot at 800 °C for a cell with anode support porosity of 32% and the corresponding best fit to Eq. (19). The fit is shown only for current density above about 0.2 A cm^{-2} since the Tafel equation is not satisfactory at too low a current density.

The first part of Table 5 gives the fitting parameters for cells in which the only parameter varied was the anode support thickness, which was varied between 0.5 and 2.45 mm, all other parameters having been fixed at the standard values. The second column gives the R_i, which varies between 0.101 and 0.148 Ω cm^2. Comparison with Table 1 shows that the ASR determined by current interruption varies between 0.095 and 0.14 Ω cm^2, in good agreement with the R_i obtained through fitting to the model (Eq. (19)). All $V(i)$ versus i traces from this set could be adequately fitted using one set of values for $D^{\text{eff}(1)}_{O_2-N_2}$, $D^{\text{eff}(2)}_{O_2-N_2}$, $D^{\text{eff}(1)}_{H_2-H_2O}$ and $D^{\text{eff}(2)}_{H_2-H_2O}$, which were respectively, 0.14, 0.04, 0.68, and 0.08 cm^2 s^{-1}. Since the only parameter varied was the anode support thickness, it is expected that the fitted transport parameters should be the same, consistent with the fitting results. Anode support and cathode current collector have greater porosities than respectively, anode interlayer and cathode interlayer. This is consistent with $D^{\text{eff}(1)}_{H_2-H_2O} > D^{\text{eff}(2)}_{H_2-H_2O}$ and $D^{\text{eff}(1)}_{O_2-N_2} > D^{\text{eff}(2)}_{O_2-N_2}$. In an earlier study, from the measurement of i_{as}, the $D^{\text{eff}}_{H_2-H_2O}$ was estimated to be ∼0.5 cm^2/s [12]. In that study, a single $D^{\text{eff}}_{H_2-H_2O}$ was assumed for the entire anode, despite the presence of two distinct layers (anode interlayer and anode support). The present curve-fitting shows that the effective diffusivity through the anode interlayer (∼0.08 cm^2 s^{-1}) is much lower than through the anode support (∼0.68 cm^2 s^{-1}), mainly due to its much lower porosity (∼23%) compared to that in the anode support (∼48%). The present estimates of ∼0.68 cm^2 s^{-1} for $D^{\text{eff}(1)}_{H_2-H_2O}$ and ∼0.08 cm^2 s^{-1} for $D^{\text{eff}(2)}_{H_2-H_2O}$, are thus reasonable. Independent measurements using an electrochemical technique for LSM porous bodies with porosity ranging between ∼15 and ∼45% showed that the corresponding $D^{\text{eff}}_{O_2-N_2}$ ranged between ∼0.03 and ∼0.12 cm^2 s^{-1} [13]. The estimated values

Table 5
Fitted parameters for the anode-supported cells

	R_i (Ω cm^2)	a	b	i_o (mA cm^{-2})	$D^{eff(1)}_{O_2-N_2}$ (cm^2 s^{-1})	$D^{eff(2)}_{O_2-N_2}$ (cm^2 s^{-1})	$D^{eff(1)}_{H_2-H_2O}$ (cm^2 s^{-1})	$D^{eff(2)}_{H_2-H_2O}$ (cm^2 s^{-1})
Anode support thickness varied (electrolyte thickness = 8 μm, anode support porosity = 48%, cathode interlayer thickness = 20 μm)								
Anode support thickness (mm)								
0.5	0.101	0.098	0.11	410	0.14	0.04	0.68	0.08
1.0	0.104	0.094	0.11	425	0.14	0.04	0.68	0.08
1.5	0.135	0.105	0.12	417	0.139	0.04	0.68	0.079
2.45	0.148	0.12	0.118	362	0.14	0.04	0.68	0.08
Electrolyte thickness varied (anode support thickness = 1.0 mm, anode support porosity = 48%, cathode interlayer thickness = 20 μm)								
Electrolyte thickness (μm)								
4	0.103	0.09	0.13	500	0.14	0.04	0.68	0.08
8	0.104	0.094	0.11	425	0.14	0.04	0.68	0.08
15	0.114	0.088	0.095	396	0.14	0.04	0.68	0.08
20	0.142	0.086	0.095	404	0.14	0.042	0.68	0.082
Anode support porosity varied (Electrolyte thickness = 8 μm, anode support thickness = 1.0 mm, cathode interlayer thickness = 20 μm)								
Anode support porosity								
32%	0.149	0.096	0.092	352	0.14	0.04	0.22	0.085
48%	0.104	0.094	0.11	425	0.14	0.04	0.68	0.08
57%	0.094	0.03	0.079	684	0.14	0.04	0.75	0.08
76%	0.08	0.022	0.09	783	0.14	0.04	0.82	0.08
Cathode interlayer thickness varied (electrolyte thickness = 8 μm, anode support thickness = 1.0 mm, anode support porosity = 48%)								
Cathode interlayer thickness (μm)								
6	0.096	0.176	0.155	321	0.135	0.04	0.61	0.08
20	0.104	0.094	0.11	425	0.14	0.04	0.68	0.08
56	0.118	0.095	0.155	543	0.135	0.04	0.61	0.08
105	0.134	0.105	0.155	598	0.138	0.04	0.63	0.08

of $D^{eff(1)}_{O_2-N_2}$ (~45% porosity) and $D^{eff(2)}_{O_2-N_2}$ (~26% porosity) from curve-fitting as ~0.14 and ~0.04 cm^2 s^{-1}, respectively, are in excellent agreement with the actual measurements. Also note that $D^{eff(1)}_{H_2-H_2O} > D^{eff(1)}_{O_2-N_2}$, consistent with expectations since $D_{H_2-H_2O} > D_{O_2-N_2}$, by virtue of the much lower molecular weight of H_2 as compared to the other species. At 800 °C, the $D_{H_2-H_2O}$ is ~7.7 cm^2 s^{-1}, estimated using the Chapman–Enskogg model [14]. The anode support porosity is ~48%. Based on the estimated $D^{eff(1)}_{H_2-H_2O}$ by curve fitting, the measured porosity, and estimated $D_{H_2-H_2O}$, a totuosity factor of ~5.4 is determined, which is quite reasonable.

Also listed in Table 5 are the corresponding a and b, which describe the net activation polarization, wherein the activation polarizations at both the anode and the cathode are lumped into one. As the activation polarizations from both electrodes are lumped into one single polarization equation, the parameters a and b are phenomenological fitting parameters, and the exchange current density obtained from these is also a phenomenological fitting parameter. These parameters using the Butler–Volmer type equation can be given by

$$a \approx -\frac{RT}{4\alpha F} \ln i_o \tag{21}$$

and

$$b \approx \frac{RT}{4\alpha F} \tag{22}$$

where α is the transfer coefficient. Thus, from Eqs. (21) and (22), the exchange current density is given in terms of the fitting parameters a and b by

$$i_o = \exp\left(-\frac{a}{b}\right) \tag{23}$$

It is important to note that for the fitting procedure and units used, there will be corresponding units for i_o, here A cm^{-2}. That is, the parameters a and b depend upon the choice of units, and thus so do the units of i_o. Thus, for example, for an anode support thickness of 0.5 mm with $a = 0.098$ and $b = 0.11$, the $i_o = (-0.098/0.11) = 0.41$ A cm^{-2} or 410 mA cm^{-2}. Table 5 shows that the estimated exchange current densities are essentially the same, about 415 mA cm^{-2} virtually for all anode support thicknesses, except for anode support thickness of 2.45 mm, for which it is somewhat lower (~362 mA cm^{-2}). The significance of the lower i_o for thick anode supports will be discussed later. Examination of Fig. 18 shows that fitted curve diverges below about 0.3 A cm^{-2}, consistent with the expectation that for current densities lower than about i_o, the Tafel equation does not satisfactorily describe activation polarization.

Table 5 also gives the fitting parameters for set of cells tested at 800 °C wherein the only parameter varied was the electrolyte thickness, all other parameters maintained at the standard values. The values of R_i obtained from the best fits vary between 0.103 and 0.142 Ω cm^2 for an electrolyte thickness ranging between 4 and 20 μm. These compare well with the ohmic ASR determined by current interruption given in Table 1, which ranges between 0.1 and 0.14 Ω cm^2. The entire set of data could be fitted well with the same values of $D^{eff(1)}_{O_2-N_2}$, $D^{eff(2)}_{O_2-N_2}$, $D^{eff(1)}_{H_2-H_2O}$, and $D^{eff(2)}_{H_2-H_2O}$, which is consis-

tent with expectations since the microstructures and porosities of the anode support, anode interlayer, cathode current collector and cathode interlayer were the same in all of these cells. The fitted parameters a and b give the magnitude of the exchange current density, i_o, which ranges between ~400 and ~500 mA cm^{-2}, the same as before.

Table 5 further gives the results of fitting data on cells wherein the only parameter varied was the anode support porosity, all other parameters fixed at the standard values. The R_i values corresponding to the best fits vary between 0.149 Ω cm^2 for anode support porosity of 32% to 0.08 Ω cm^2 for anode support porosity of 76%. As shown in Table 1, the ohmic ASR obtained using current interruption for the same porosity range varies between 0.156 and 0.074 Ω cm^2, indicating good agreement. The transport parameters corresponding to the cathode current collector, $D^{\text{eff}(1)}_{O_2-N_2}$, cathode interlayer, $D^{\text{eff}(2)}_{O_2-N_2}$, and anode interlayer, $D^{\text{eff}(2)}_{H_2-H_2O}$, are essentially the same as before, consistent with expectations since the respective microstructures of these regions were the same in all cells tested. Note, however, that the $D^{\text{eff}(1)}_{H_2-H_2O}$, which is the effective diffusivity through the anode support, varies between 0.22 cm^2 s^{-1} for a cell with anode support porosity of 32% to 0.82 cm^2 s^{-1} for anode support porosity of 76%. The profound effect of anode support porosity on H_2–H_2O gaseous transport and the corresponding anodic concentration polarization is evident. The parameters, which describe activation polarization, namely a and b, are also listed in Table 5. It is interesting to note that the estimated exchange current density, i_o, varies between ~352 mA cm^{-2} for anode support porosity of 32%, to ~783 mA cm^{-2} for anode support porosity of 76%. This result leads to the following observations/conclusions. (1) The fact that changes made on the anode side affect the overall exchange current density, i_o, suggests that there must be significant contribution from both the cathode and the anode to the net activation polarization. (2) The anode interlayer, where most of the anodic electrochemical reaction occurs, was the same in all cells. Yet the anodic activation polarization appears to be affected. This apparent conflict can be resolved when the factors which influence activation polarization are examined more closely. It is to be noted that activation polarization is a function of the concentration (partial pressure) of the electro-active species in the region of the electrode where electrochemical reactions occur (i.e., in the interlayer); the higher the concentration (partial pressure) of the electro-active species, the higher should be the exchange current density, i_o, and the lower should be the activation polarization. For a given imposed current density, the lower is the anode support porosity, the lower will be $p_{H_2(i)}(i)$ and $p'_{H_2(i)}(i)$, the lower will be the exchange current density, i_o, and the higher will be the activation polarization. That is, the activation polarization is not independent of concentration polarization. For this reason, as the anode support porosity is decreased, there also is an effect on the estimated i_o. The observation that for a cell with anode support thickness of 2.45 mm the exchange current density was lower than for thinner anode supports, is also consistent with this reasoning. The implication is that Eq. (18), which has been used to describe the overall $V(i)$ versus i polarization behavior is rather crude, since it ignores the dependence of a and b on the partial pressures of the electro-active species; for the anode side $p_{H_2(i)}(i)$ and $p'_{H_2(i)}(i)$, and for the cathode side $p_{O_2(i)}(i)$ and $p'_{O_2(i)}(i)$. This also implies that more complex models which incorporate the complete Butler–Volmer equation, such as in the work of Zhu and Kee, may be required to demonstrate better quantitative agreement [10].

Table 5 gives the results of curve fitting for cell tests wherein the cathode interlayer thickness was varied between ~6 and ~105 μm, all other parameters fixed at the standard values. Once again the values of $D^{\text{eff}(1)}_{O_2-N_2}$, $D^{\text{eff}(2)}_{O_2-N_2}$, $D^{\text{eff}(1)}_{H_2-H_2O}$, and $D^{\text{eff}(2)}_{H_2-H_2O}$ corresponding to the best fits are essentially the same as for all other cells with the same microstructures and porosities (that is the standard cells, those with different electrolyte thicknesses, and cells with different anode support thicknesses). The ohmic ASR values from the data fit are also consistent with those determined by current interruption. From the fitted parameters a and b, the estimated exchange current density, i_o, for cathode interlayer thickness of ~6 μm is about 321 mA cm^{-2}, which is the lowest. For cathode interlayer thickness of 20 μm, the i_o is ~425 mA cm^{-2}, while it increases to over 500 mA cm^{-2} for cathode interlayer thicknesses of 56 and 105 μm. Theoretical analysis by Tanner et al. [15] for a composite electrode shows that effective charge transfer resistance is given by

$$R_{\text{ct(eff)}} \approx \sqrt{\frac{\rho_i d R^o_{\text{ct}}}{1 - V_v}} \tag{24}$$

where R^o_{ct} is the intrinsic charge transfer resistance (which is representative of the electrocatalyst spread evenly on a planar electrolyte surface), ρ_i is the ionic resistivity of the composite electrode and d is the grain size. The measured effective exchange current density, alternatively, can be given by

$$i_o \approx \frac{RT}{4F}\sqrt{\frac{1 - V_v}{\rho_i R^o_{\text{ct}} d}} \tag{25}$$

Both of these two Eqs. (24) and (25), are asymptotic limits of the general equations given by Tanner et al. [15], which shows that as the electrode interlayer thickness, h, increases, the exchange current density increases (or effective charge transfer resistance decreases), and for $h \geq 10d$–$15d$ reaches an asymptotic value given by Eq. (25) (or Eq. (24)). In the present experiments, the typical grain size in the cathode interlayer was ~2 μm. Hence, it is expected that for an interlayer thickness above about 20–30 μm, the asymptotic value would be achieved. The observation that the exchange current density increases with increasing cathode interlayer thickness is consistent with this model. Note that the i_o seems to reach an asymptotic value for cathode interlayer thickness of ~50 μm. An interesting observation is that even though the cell with 20 μm cathode interlayer has a lower i_o than the cell

with ∼56 μm cathode interlayer, it exhibits higher power density. This is consistent with the fact that the cell with 56 μm thick cathode interlayer exhibits higher ohmic ASR, which seems to arise from the cathode interlayer. In addition, the larger the cathode interlayer thickness, the higher is the cathodic concentration polarization. The model by Tanner et al. does not account for ohmic losses in the cathode interlayer, which can occur due to inhomogeneous distribution of particles present in real composite electrodes [15].

4.3. Temperature dependence of polarization

The ohmic polarization is temperature dependent mainly by virtue of the thermally activated dependence of the YSZ ionic resistivity; the lower the temperature, the higher is the resistivity. Note that the ASR for the standard cells at 800 °C is 0.104 Ω cm^2 while that at 700° C is 0.19 Ω cm^2. The activation polarization is also thermally activated; which is reflected in the thermally activated dependence of the exchange current density i_o through two temperature-dependent parameters, namely, ρ_i and R^o_{ct}. The concentration polarization, however, is weakly dependent on temperature. There are two sources of temperature dependence of concentration polarization. One of them is the temperature dependence of the partial pressure of hydrogen at the anode interlayer/electrolyte interface (Eq. (8)), $p'_{H_2(i)}(i)$, and partial pressure of oxygen at the cathode interlayer/electrolyte interface (Eq. (13)), $p'_{O_2(i)}(i)$, which exhibit temperature dependence directly as well as through the temperature dependence of effective diffusivities. The binary diffusivities, through the Chapman-Enskogg equation are proportional to $T^{3/2}$. The other dependence is direct linear relationship with temperature, as reflected in Eq. (7) for $\eta_{a,con}$ and Eq. (18) for $\eta_{c,con}$. The temperature dependence of concentration polarization thus is generally weak. Calculations of $\eta_{a,con}$ and $\eta_{c,con}$ made using Eqs. (7) and (18), respectively, show that these are weakly dependent on temperature over the temperature range between 600 and 800 °C. Fig. 19, for example, shows calculated $\eta_{a,con}$ as a function of current density over a range of temperatures between 600 and 800 °C. Note that the $\eta_{a,con}$ slightly increases with temperature. Thus, the principal temperature dependence of cell performance is due to the temperature dependence of ohmic and activation polarizations.

4.4. Estimation of anode and cathode-limiting current densities and concentration polarization as a function of various cell parameters

From the estimated $D^{eff(1)}_{O_2-N_2}$, $D^{eff(2)}_{O_2-N_2}$, $D^{eff(1)}_{H_2-H_2O}$, and $D^{eff(2)}_{H_2-H_2O}$ from curve-fitting to $V(i)$ versus i data, the i_{as} and i_{cs} were estimated using Eqs. (10) and (14), respectively, for cells with different anode support thicknesses and anode support porosities. The estimated i_{as} and i_{cs} are listed in Table 6. Using the $D^{eff(1)}_{H_2-H_2O}$ and $D^{eff(2)}_{H_2-H_2O}$, anode concentration polarization was calculated for a number of cases. Also calculated

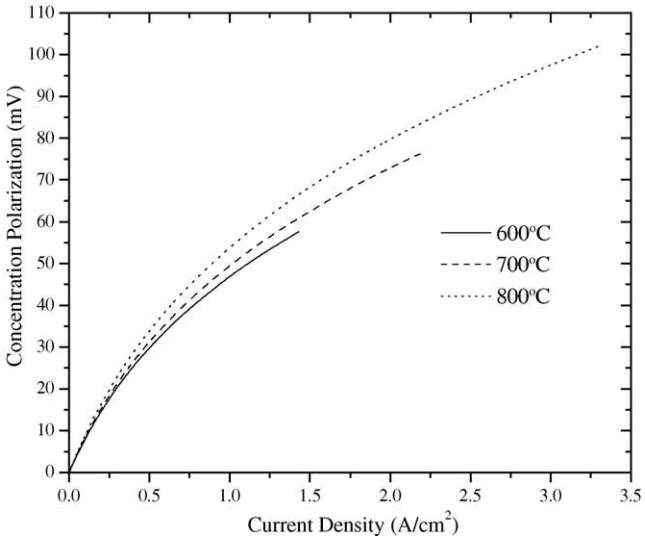

Fig. 19. Anode concentration polarization for the cell with optimized parameters (0.5 mm anode support thickness, 57% anode support porosity) as a function of current density over a temperature range between 600 and 800 °C.

was the partial pressure of hydrogen at the electrolyte/anode interlayer interface, $p'_{H_2(i)}(i)$. Plots of the calculated $p'_{H_2(i)}(i)$ and $\eta_{a,con}$ versus i are given in Fig. 20 for anode support thickness ranging between 0.5 and 2.45 mm. The profound effect of anode support thickness on anodic concentration polarization is clearly seen in the figure. Thus, making the anode support as thin as possible is important, although from the standpoint of mechanical ruggedness, probably the lower limit is about 0.5 mm. It is also to be noted that the decrease in $p'_{H_2(i)}(i)$ at higher anode support thicknesses leads to higher activation polarization since a and b are functions of partial pressures of hydrogen (at the anode interlayer/electrolyte interface). Fig. 21 shows similar plots of $p'_{H_2(i)}(i)$ and $\eta_{a,con}$ versus i where the parameter varied was the anode support porosity. Note the large effect of anode support porosity, especially at low values of porosity. In Figs. 20 and 21, the vertical scale on the left axis is in mV. Note that concentration polarization as high as ∼150 mV (or even greater) is estimated at high current densities. Fig. 22 shows similar plots of $p'_{O_2(i)}(i)$ and $\eta_{c,con}$ versus i for the case where the only param-

Table 6
Limiting current densities for various anode thicknesses and anode porosities

	i_{as} (A cm^{-2})	i_{cs} (A cm^{-2})
Anode thickness (mm)		
0.5	21.81	12.8
1.0	12.49	
1.5	8.75	
2.45	5.58	
Anode porosity (%)		
32	4.49	
48	12.49	
57	13.57	
76	14.63	

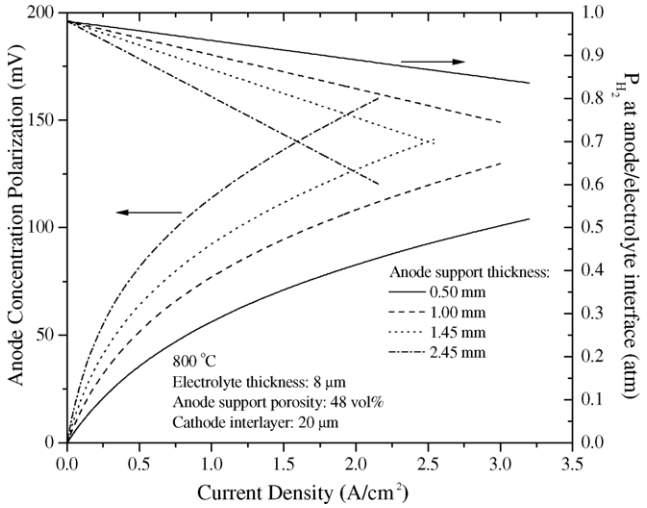

Fig. 20. Anode concentration polarization, $\eta_{a,conc}$, and partial pressure of hydrogen at the anode interlayer/electrolyte interface, $p'_{H_2(i)}(i)$, as a function of current density for cells with different anode support thicknesses.

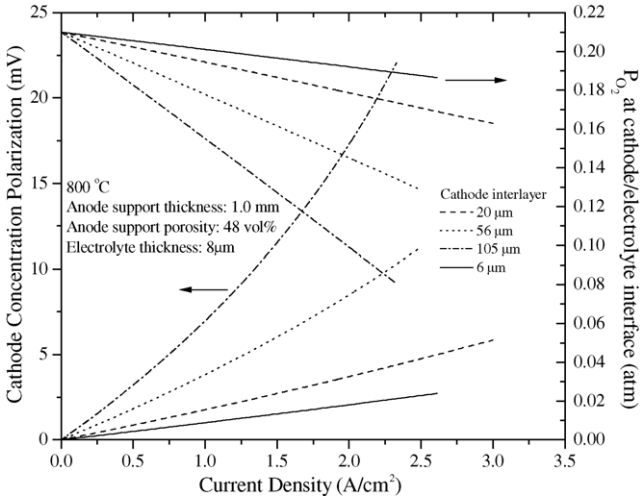

Fig. 22. Cathode concentration polarization, $\eta_{c,conc}$, and the partial pressure of oxygen at cathode interlayer/electrolyte interface, $p'_{O_2(i)}(i)$, as a function of cell current density for cells with different cathode interlayer thicknesses.

eter varied was the cathode interlayer thickness. In general, the cathodic concentration polarization is small as long as the cathode interlayer thickness is small. However, for large cathode interlayer thicknesses (e.g. ~50–100 μm), the $\eta_{c,con}$ was estimated to be as high as ~20 mV. Especially significant is the fact that the corresponding $p'_{O_2(i)}(i)$ can be substantially lower than $p^o_{O_2}$, which thus also increases activation polarization, since *a* and *b* depend upon on $p'_{O_2(i)}(i)$. Thus, even in an anode-supported cell, it is important to ensure that oxidant transport through the cathode is not impeded.

4.5. The optimized cell

Using the maximum power density (MPD) as a figure of merit, note that the optimized cell exhibited an MPD of ~1.8 W cm^{-2} at 800 °C, ~0.8 W cm^{-2} at 700 °C and ~0.4 W cm^{-2} at 600 °C. All three polarization losses were proportionately lower in the optimized cell as compared to the standard cell which exhibited MPD of ~1.2 W cm^{-2} at 800 °C, ~0.58 W cm^{-2} at 700 °C and ~0.2 W cm^{-2} at 600 °C. In the present work, only few parameters were varied, namely the various thicknesses, and anode support porosity. It is clear that further performance gains are to be expected when the dependence of various polarization losses on other parameters is examined, such as the relative proportions of the phases in the composite electrodes, and microstructures of the electrodes. The observation that even within a given materials set the cell performance can be varied over a wide range exemplifies the role of various parameters on polarizations, and underscores the importance of investigating the role of microstructural and geometric parameters. It also suggests that when investigating the effect of various materials on cell performance, a comparison among different materials by itself may be of little value, unless a careful study of the microstructural and geometric parameters is also made concurrently.

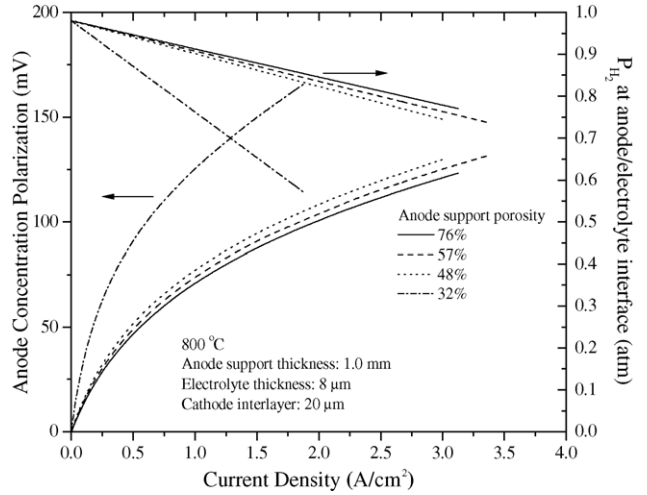

Fig. 21. Anode concentration polarization $\eta_{a,conc}$, and partial pressure of hydrogen at the anode interlayer/electrolyte interface, $p'_{H_2(i)}(i)$, as a function of current density for cells with different anode support porosities.

5. Summary

In the present work, a series of anode-supported cells comprising a mixture of Ni + YSZ anode support, Ni + YSZ anode interlayer, YSZ electrolyte, LSM + YSZ cathode interlayer, and LSM cathode current collector, were fabricated with one parameter varied at a time. The cell parameters investigated were the electrolyte thickness, the anode support thickness, the cathode interlayer thickness, and anode support porosity. Electrochemical performance was measured with humidified hydrogen as fuel and air as oxidant over a temperature range from 600 to 800 °C, with most of the

testing done at 800 °C. The ohmic ASR was measured by current interruption. It was observed that the various polarizations and ohmic ASR are functions of the cell parameters investigated. The electrochemical performance of cells was fitted to a simple analytical model. The emphasis was on describing voltage versus current density performance curves with the minimum possible number of parameters, which in principle can be independently measured. The results showed that a significant contribution to the ohmic ASR is attributed to components other than the electrolyte at temperatures as low as 700 °C, as long as the electrolyte thickness is small (∼10 μm). This shows that YSZ as electrolyte is satisfactory in a thin film form down to at least 700 °C, and perhaps down to 600 °C. Through the optimization study, a set of parameters was identified, an optimized cell was fabricated and its electrochemical performance was evaluated. The maximum power density of the optimized cell was $\sim 1.8\,W\,cm^{-2}$ at 800 °C and $\sim 0.4\,W\,cm^{-2}$ at 600 °C. The results show that a significant improvement in cell performance can be realized by addressing microstructural and geometric aspects of cell parameters, even when using the standard set of materials (LSM, YSZ, and Ni). Further performance gains are to be expected with optimization of other cell parameters, which include the anode interlayer thickness, cathode current collectors and also the relative proportions of phases in the composite electrodes. It is clear that even greater improvements are possible using materials with intrinsically superior properties. The present study underscores the importance of microstructural and geometric parameters, and the need to carry out a quantitative optimization study for a given materials set.

Acknowledgments

This work was supported by the U.S. Department of Energy, NETL contract no. DE-AM26-99FT40463, through a subcontract from Parsons Infrastructure and Technology Group, Inc. to the University of Utah. The authors appreciate the assistance of Dr. Yi Jiang in testing some of the cells.

References

[1] J.W. Kim, A.V. Virkar, K.-Z. Fung, K. Metha, S.C. Singhal, Polarization effects in intermediate temperature, anode-supported solid oxide fuel cells, J. Electrochem. Soc. 146 (1) (1999) 69.
[2] S. Desouza, S.J. Visco, L.C. DeJonghe, Reduced-temperature solid oxide fuel cell based on YSZ thin-film electrolyte, J. Electrochem. Soc. 144 (1997) L35.
[3] T. Tsai, S.A. Barnett, Increased solid-oxide fuel cell power density using interfacial ceria layers, Solid State Ionics 98 (1997) 191.
[4] E.E. Underwood, Quantitative Stereology, Addison-Wesley, Reading, MA, 1970.
[5] F. Zhao, Y. Jiang, G.Y. Lin, A.V. Virkar, in: H. Yokokawa, S.C. Singhal (Eds.), The effect of electrode microstructure on cathodic polarization, Proceedings of the Seventh International Symposium on Solid Oxide Fuel Cells, The Electrochemical Society, Pennington, NJ, 2001, p. 501, PV2001-16.
[6] K. Sasaki, J.-P. Wurth, R. Gschwend, M. Godickemeier, L.J. Gauckler, Microstructure-property relations of solid oxide fuel cell cathodes and current collectors, J. Electrochem. Soc. 143 (1996) 530.
[7] H. Tagawa, J. Mizusaki, Y. Arai, Y. Kuwayama, S. Tsuchiya, T. Takeda, S. Sekido, Sinterability and electrical conductivity of variously prepared perovskite-type oxide, $La_{0.5}Sr_{0.5}CoO_3$, Denki Kagaku 58 (1990) 512.
[8] S. Mizuta, K. Shirasawa, Y. Suzuki, The effect of water and porosity on ionic conduction of sintered barium fluoride, Denki Kagaku 41 (1973) 913.
[9] T. Takahashi, Y. Suzuki, Effect of porosity on electrical conductivity of sintered $(ZrO_2)_{0.9}(Y_2O_3)_{0.1}$, Denki Kagaku 37 (1969) 782.
[10] H. Zhu, R.J. Kee, A general mathematical model for analyzing the performance of fuel-cell membrane-electrode assemblies, J. Power Sources 117 (2003) 61–74.
[11] M.A. Khaleel, J.R. Selman, Cell, stack and system modeling, in: S.C. Singhal, K. Kendall (Eds.), High Temperature Solid Oxide Fuel Cells, 2003, p. 291.
[12] Y. Jiang, A.V. Virkar, Fuel composition and diluent effect on gas transport and performance of anode-supported SOFCs, J. Electrochem. Soc. 150 (7) (2003) A942–A951.
[13] F. Zhao, T.J. Armstrong, A.V. Virkar, Measurement of O_2–N_2 effective diffusivity in porous media at high temperatures by using an electrochemical cell, J. Electrochem. Soc. 150 (3) (2003) A249–A256.
[14] E.L. Cussler, Diffusion: Mass Transfer in Fluid Systems, Cambridge University Press, Cambridge, 1995.
[15] C.W. Tanner, K-Z. Fung, A.V. Virkar, The effect of porous composite electrode structure on solid oxide fuel cell performance. I. Theoretical analysis, J. Electrochem. Soc. 144 (1) (1997) 21–30.